The formation of supersaturated solid solutions in Fe–Cu alloys deformed by high-pressure torsion

A. Bachmaier [a,*], M. Kerber [b], D. Setman [b], R. Pippan [a]

[a] *Erich Schmid Institute of Materials Science, Austrian Academy of Sciences, Jahnstr. 12, A-8700 Leoben, Austria*
[b] *Research Group Physics of Nanostructured Materials, University of Vienna, Boltzmanngasse 5, A-1090 Vienna, Austria*

Abstract

Fully dense bulk nanocomposites have been obtained by a novel two-step severe plastic deformation process in the immiscible Fe–Cu system. Elemental micrometer-sized Cu and Fe powders were first mixed in different compositions and subsequently high-pressure-torsion-consolidated and deformed in a two-step deformation process. Scanning electron microscopy, X-ray diffraction and atom probe investigations were performed to study the evolving far-from-equilibrium nanostructures which were observed at all compositions. For lower and higher Cu contents complete solid solutions of Cu in Fe and Fe in Cu, respectively, are obtained. In the near 50% regime a solid solution face-centred cubic and solid solution body-centred cubic nanograined composite has been formed. After an annealing treatment, these solid solutions decompose and form two-phase nanostructured Fe–Cu composites with a high hardness and an enhanced thermal stability. The grain size of the composites retained nanocrystalline up to high annealing temperatures.
© 2011 Acta Materialia Inc. Published by Elsevier Ltd. Open access under CC BY-NC-ND license.

Keywords: High-pressure torsion; Solid solubility extension; Fe–Cu alloy

1. Introduction

Due to novel properties of materials fabricated out of typically immiscible alloys, like high thermal and electrical conductivity and excellent magnetic properties (i.e. high magnetoresistance and coercivity), a long-standing interest in the preparation of such alloys exists [1–3]. The formation of metastable phases in alloy systems with a negative heat of mixing as well as positive heat of mixing has been intensively investigated in recent years [3–6]. Since the 1990s, the formation of metastable single-phase solid solutions with nanocrystalline grain sizes for mechanically alloyed Fe–Cu powders has been studied extensively by several research groups [7–13]. The Fe–Cu system, a spinodal type system, is nearly immiscible in equilibrium at room temperature and up to 600 °C and has a positive heat of mixing [14]. Due to mechanical alloying, the potential to extend the mutual solubility of Fe and Cu has been widely reported due to friction and strong impacts of the steel balls on the powder grains. The formation of face-centred cubic (fcc) single-phase solid solutions is observed for Fe_xCu_{1-x} alloys with a Fe content $x < 60$ at.%, two-phase alloys consisting of a fcc and a body-centred cubic (bcc) phase are formed for a Fe content of $60 < x < 80$ at.% and bcc single-phase solid solutions are obtained for a Fe content of $x > 80$ at.% [8–10]. The mixing occurs on the atomic level in the milled alloys, which was confirmed by Mössbauer spectroscopy [8,11]. The crystallite size in the milled powders is reported to be ∼20 nm or even smaller. Decomposition of the unstable FeCu solid solutions occurred due to annealing treatments as reported in several studies [10–12].

In this study, a new approach to obtain fully dense homogeneous bulk Fe–Cu composites by high-pressure torsion (HPT) deformation is presented. Sauvage et al. showed that by HPT deformation the production of a non-equilibrium Cu supersaturated solid solution in a

---

* Corresponding author. Tel.: +43 3842 804 314; fax: +43 3842 804 116.
 E-mail address: andrea.bachmaier@stud.unileoben.ac.at (A. Bachmaier).

Cu–Fe composite was possible [15,16]. Many structural defects are incorporated in a material during severe plastic deformation (SPD) processes, which is accompanied with a higher dislocation density, a higher vacancy concentration and the continuous formation of new grain boundaries [15–18]. A Cu–Fe composite with an inhomogeneous layered nanostructured microstructure was produced, where nano-scaled Fe clusters dissolved into the Cu matrix.

Instead of a filamentary composite starting material, micrometer-sized Fe and Cu powders are used, which is similar to the mechanical alloying process. Nevertheless, the product after mechanical alloying is a powder and further processes like compaction and sintering are necessary to obtain bulk specimens. One emerging disadvantage is that the nanocrystalline structure can be lost during these treatments and decomposition of the supersaturated solid solutions occurs during annealing. Furthermore, an increase of the impurity content is unavoidable. The advantage of the HPT process is that the end product is directly available as a massive bulk material. Up to now it was impossible to generate homogeneous nanocrystalline supersaturated FeCu composites by HPT or equal angular channel pressing micrometer-sized powder consolidation. One of the goals in this study was to find a way to overcome these problems. If nanocrystalline supersaturated Fe–Cu composites with homogeneous microstructures can be produced by HPT deformation, it would be an easy way to produce such composites, which are also very interesting materials for magnetic applications. Fcc supersaturated solid solutions are ferromagnetic for a Fe content of $x > 15$. Furthermore, nanocrystalline Fe–Cu composites with small amounts of Cu should exhibit large magnetostrictive effects [19–21].

2. Experimental

Commercial copper powders (99.9% purity, $-170 + 400$ mesh) and iron powders (99.9% purity, $-100 + 200$ mesh) were used as starting materials. These micrometer-sized powders were mixed in different ratios to obtain powder mixtures with final alloy compositions of $Fe_{100-x}Cu_x$ ($x = 15, 30, 50, 85$). The powder mixtures were precompacted and deformed in our large HPT tool which can be used to deform samples up to a diameter of 50 mm and a thickness of about 10 mm. Afterwards, new smaller HPT

samples were cut out of the previously deformed sample. Therefore, the sample was cut at a radius of 5 and 15 mm, a cylindrical rod was turned from the cut part and slices of ~0.8 mm thickness were cut from this rod. These "new" HPT samples were deformed a second time. The reason for this special procedure will be discussed later. The single steps of the sample production are illustrated in the schematic sketch in Fig. 1. Further information about HPT deformation and a detailed description of the HPT equipments are given in Refs. [22–24]. A list of the deformation parameters of both processing steps for all samples deformed in this study is given in Table 1. Different deformation parameter sets were used for sample processing in order to generate a nanostructure relatively quickly, taking into account the limitation of the torque of the larger HPT device.

All microstructural investigations were performed at a radius of 10 mm of the HPT sample after the first deformation step and at a radius of 3 mm after the second deformation step in the tangential direction with a scanning electron microscope (SEM) type LEO 1525 using backscattered electrons. The direction of the SEM observations is also shown in Fig. 1. Vickers microhardness measurements were performed on a BUEHLER Mircomet 5100 using a load of 500 g. Indents were made across the radii of the samples with a distance of 0.25 mm between the indents on the 8 mm diameter disks after the cutting procedure described above. After the first processing step, nearly constant hardness values were measured across the radii of the samples and the mean values of 32 indents over the radii of the samples are given. In contrast, mean values of 16 indents starting from a radius of 2 mm to the outer edge of the sample are reported after the second processing step in this study, which corresponds to the saturation region. X-ray diffraction measurements were taken with an AXS BRUKER D8 system in Bragg–Brentano θ–2θ geometry using Co (K_α) radiation using a spot size of 0.5 mm and rotating the sample around the surface normal to compensate for possible texture effects. Furthermore an atom probe analysis has been carried out on the $Fe_{50}Cu_{50}$ sample. Bars with a dimension of $0.3 \times 0.3 \times 3$ mm were cut out of the HPT deformed sample. A two step electrochemical polishing procedure was used to get finally tips situated at a radius of 3 mm referred to the HPT sample. The atom probe analysis was conducted on a LEAP 3000X HR from
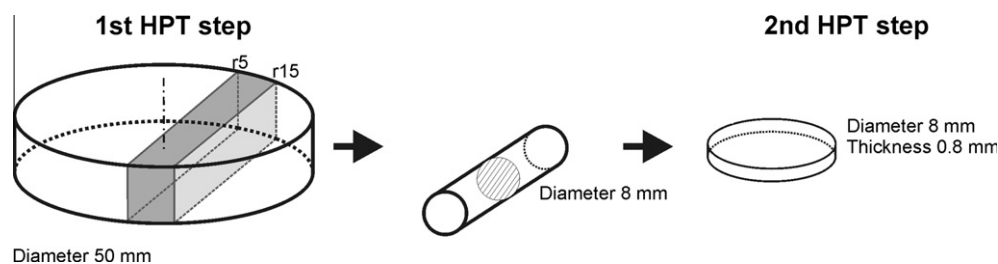

Fig. 1. Schematic sketch of the individual sample production and deformation steps: from the sample (diameter of 50 mm) deformed in the first HPT deformation step, new samples (diameter of 8 mm) are cut and further HPT deformation is conducted.

Table 1
Deformation parameters of the first and second deformation steps for all deformed samples in this study.

	(1) Deformation step			(2) Deformation step		
	# Rotations	Thickness (mm)	$\varnothing$ (mm)	# Rotations	Thickness (mm)	$\varnothing$ (mm)
$Fe_{85}Cu_{15}$	10	9.5	50	50	0.5	8
$Fe_{70}Cu_{30}$	10	9.5	50	100	0.6	8
$Fe_{50}Cu_{50}$	20	9.6	50	200	0.5	8
$Fe_{15}Cu_{85}$	20	11.5	50	100	0.5	8

Cameca®, formerly Imago Scientific Instruments. The sample was measured with a pulsed laser with a frequency of 250 kHz, a temperature of 40 K and a laser pulse energy of 0.5 nJ. The software package IVAS 3.4.3 from Cameca® was used for reconstruction of the probed volume and the data analysis.

Differential scanning calorimetry (DSC) with a Perkin Elmer DSC-7 was performed to evaluate the decomposition temperature of the FeCu alloys with 10 °C min^{-1} of heating rate up to a temperature of 590 °C on ring samples (inner diameter 2 mm, outer diameter 3 mm) cut out of the samples after both deformation steps.

3. Results

3.1. Formation of supersaturated solid solutions

After powder mixing to obtain the different compositions ($Fe_{85}Cu_{15}$, $Fe_{70}Cu_{30}$, $Fe_{50}Cu_{50}$ and $Fe_{15}Cu_{85}$) and precompaction of the powder mixtures directly in the

HPT tool, the precompacted samples with a diameter of 50 mm were HPT deformed for 10–20 rotations. Fig. 2 shows the microstructure of the $Fe_{70}Cu_{30}$ and $Fe_{85}Cu_{15}$ samples after the deformation at a lower and at a higher magnification. Due to the lower scattering factor of the Fe phase, the Cu-rich regions appear brighter in the backscatter electron mode and the Fe and Cu regions can be easily distinguished. Continuous bands of Cu-rich regions (thickness 1–2 μm) are embedded in the Fe matrix and the Cu and Fe phases are not homogeneously distributed in the case of the $Fe_{85}Cu_{15}$ alloy. The thickness of the Cu bands is about ten times smaller than the particle size of the Cu powder in the initial state but the distance between the Cu bands differs a lot. From the micrograph with the higher magnification, an average grain size of 300 and 200 nm for the Fe and Cu phases in the $Fe_{85}Cu_{15}$ composite can be estimated using the backscattered electron mode. In the $Fe_{15}Cu_{85}$ composite, similar grain sizes are observed (300 nm for Cu, 300 nm for Fe). In the $Fe_{70}Cu_{30}$ composite, the Cu and Fe phase can also be differentiated very easily. From the micrograph with the higher magnification, Fe and Cu grains with a similar grain size of ∼300 nm and 200 nm can be seen. In the $Fe_{50}Cu_{50}$ composite, the grain sizes in the Cu and Fe phase are again similar (about 300 nm for Cu and 400 nm for Fe).

In Fig. 3, the final microstructures of the $Fe_{85}Cu_{15}$, $Fe_{70}Cu_{30}$, $Fe_{50}Cu_{50}$ and $Fe_{15}Cu_{85}$ samples after the second processing step are shown. Compared to the obtained microstructures after the first processing step, the grain size is significantly reduced in all four samples. In the $Fe_{85}Cu_{15}$, $Fe_{50}Cu_{50}$ and $Fe_{15}Cu_{85}$ samples an apparent homogeneous microstructure is obtained. The $Fe_{15}Cu_{85}$ sample shows a
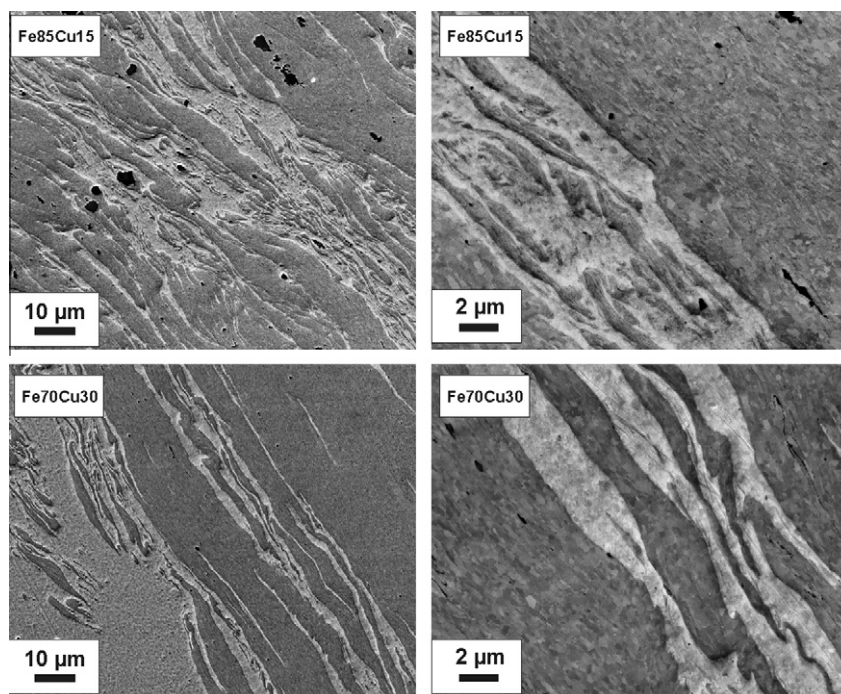
Fig. 2. SEM micrographs (backscattered electron mode) showing the microstructure of the $Fe_{85}Cu_{15}$ and the $Fe_{70}Cu_{30}$ after the first deformation step with a low and high magnification recorded at a radius of 10 mm in the tangential direction. Fe-rich regions appear darker in the image, Cu regions brighter.
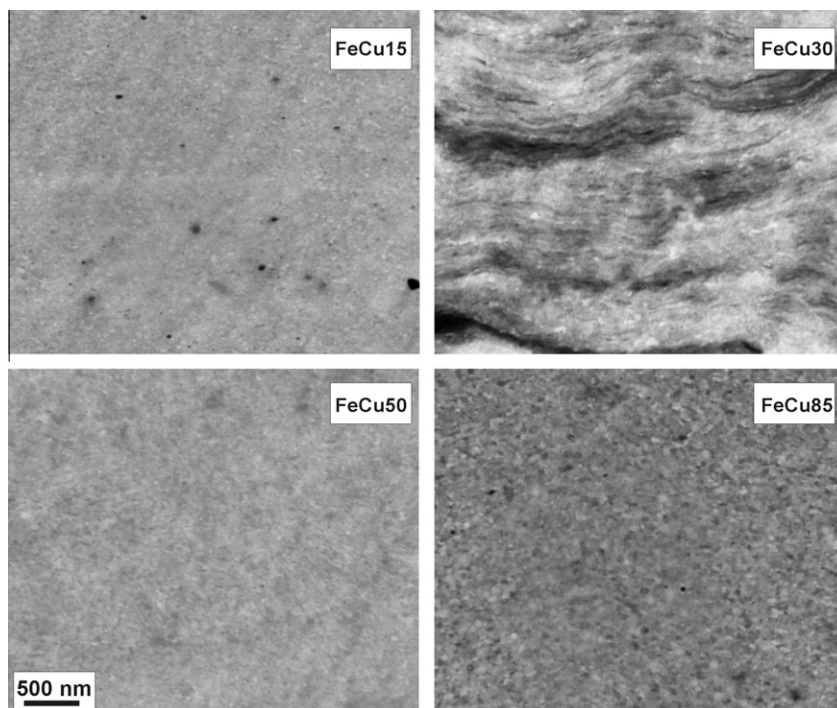
Fig. 3. SEM micrographs (backscattered electron mode) showing the final microstructure after both processing steps in all alloys ($Fe_{85}Cu_{15}$, $Fe_{70}Cu_{30}$, $Fe_{50}Cu_{50}$, $Fe_{15}Cu_{85}$) recorded at a radius of 3 mm in the tangential direction. The magnification is the same in all images.

somewhat larger grain size compared to the other microstructures but still a nanocrystalline microstructure is obtained. In the $Fe_{70}Cu_{30}$ sample, an inhomogeneous layered microstructure can be seen. The darker regions are Fe-rich regions whereas the brighter regions are Cu-rich regions. Very thin Fe layers with a thickness significantly below 50 nm are drawn trough the Cu matrix and vice versa. The grain size is nanocrystalline as well.

The mean microhardness values of the samples after the first and second processing step can be seen in Fig. 4. The first step of the HPT deformation leads to a hardness of 187 HV for the composite with the highest Cu content. Decreasing the Cu content increases the hardness after the first processing step up to a value of 341 HV for the $Fe_{85}Cu_{15}$ composite. After the second processing step, microhardness values increased nearly twice in all samples. Between the $Fe_{50}Cu_{50}$ and $Fe_{70}Cu_{30}$ samples, nearly no hardness difference exists.

From the micrographs, it is not possible to distinguish between Fe and Cu phases in the case of the $Fe_{85}Cu_{15}$, $Fe_{50}Cu_{50}$ and $Fe_{15}Cu_{85}$ samples. Therefore, X-ray diffraction investigations were performed to study the occurring phases after the first and second deformation step at the positions mentioned earlier. In Fig. 5, X-ray diffraction patterns for all four alloy compositions after the first and second deformation step are shown. In the X-ray diffraction pattern of the $Fe_{85}Cu_{15}$ alloy, peaks of the fcc Cu phase and the bcc Fe phase are visible after the first deformation step (Fig. 5a). Peaks from the composite phase are not visible within the resolution of the diffractometer but
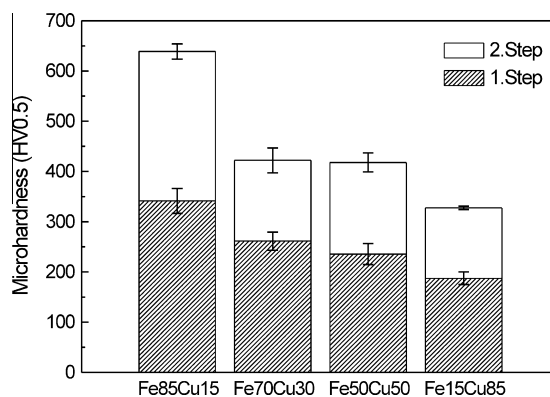

Fig. 4. Microhardness of the FeCu samples after the first and second deformation step. Mean values of 32 indents over the radii of the samples after the first processing step and mean values of 16 indents starting from a radius of 2 mm to the outer edge of the samples after the second processing step are given.

could be resolved using a high-resolution diffractometer and a highly monochromatic source. This result is consistent with the microstructure of this alloy, which shows a composite structure in the micrograph consisting obviously of Fe and Cu (Fig. 2). In general, no peaks from oxides or other contaminants are observed in all diffraction patterns. After the second deformation step, the X-ray diffraction pattern of the $Fe_{85}Cu_{15}$ alloy contains only peaks of the bcc Fe phase although slightly shifted. Therefore, we assume that supersaturated solid solution of Cu in Fe is formed after this processing step. Furthermore, both bcc
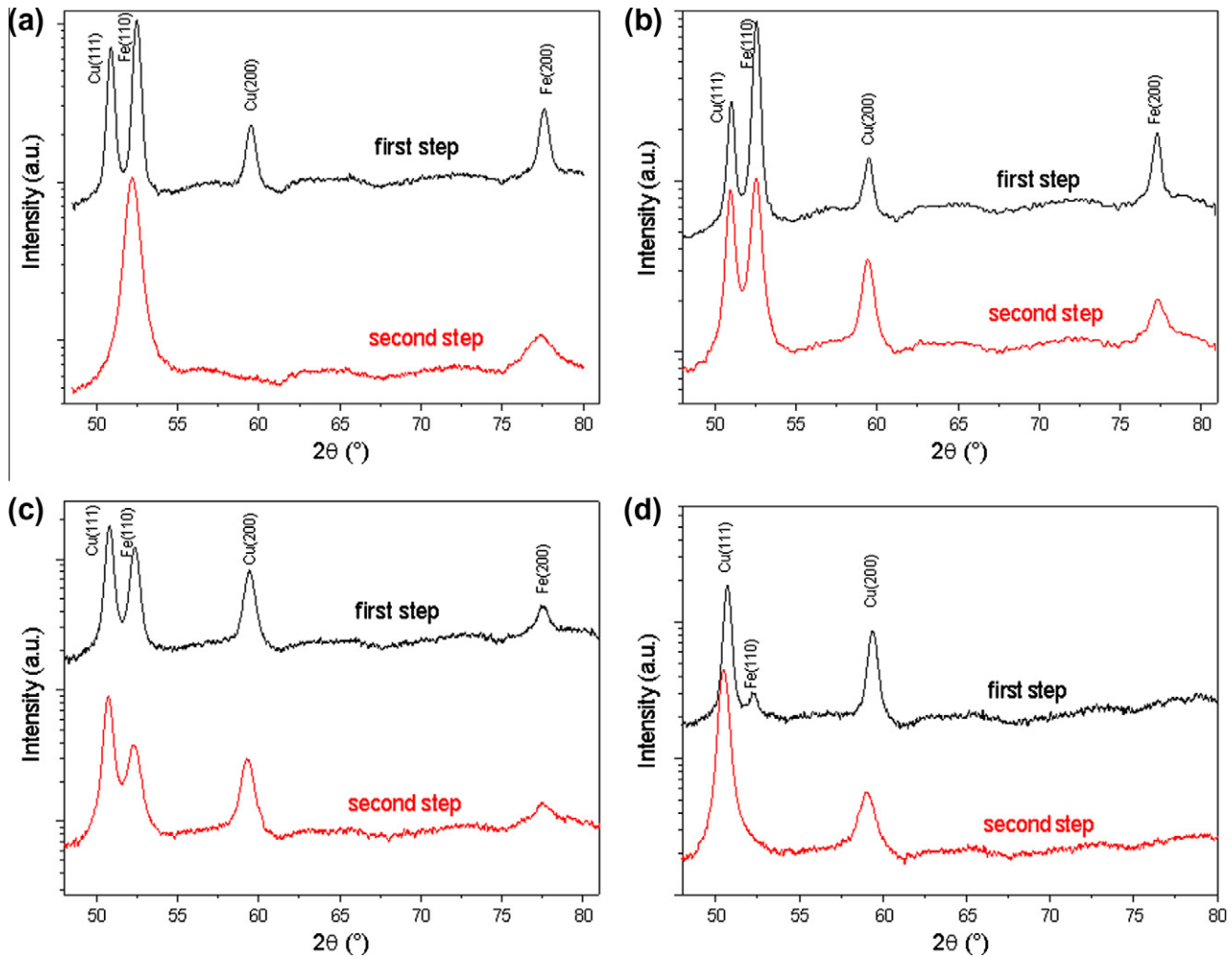
Fig. 5. X-ray diffraction patterns after the first deformation step and second deformation step of the $Fe_{85}Cu_{15}$ alloy (a), the $Fe_{70}Cu_{30}$ alloy (b), the $Fe_{50}Cu_{50}$ alloy (c) and the $Fe_{15}Cu_{85}$ alloy (d), respectively.

Fe peaks have significantly broadened due to the reduction of the mean grain size, as confirmed from the micrographs of the microstructure after the first and second deformation step. Moreover, the intensity of the Fe (110) peak increased. The Fe peaks are also shifted to lower angles compared to those recorded after the first deformation step, which might be due to the formation of a Cu solid solution in Fe. Fig. 5d shows the X-ray diffraction pattern of the $Fe_{15}Cu_{85}$ alloy. After the first deformation step, fcc Cu peaks and a weak Fe (110) peak are visible. After the second deformation step, the intensity of the Cu (111) peak increased significantly. The Fe peaks completely disappeared and only Cu peaks remain, and vice versa as in the case of the $Fe_{85}Cu_{15}$ alloy. In the $Fe_{15}Cu_{85}$ alloy, the Cu (111) peak is now shifted to lower diffraction angles, which might now be due to the formation of supersaturated Fe solid solution in the Cu phase. Furthermore, some peak broadening is also observed, which is again due to the reduction of the mean grain size.

In the X-ray diffraction patterns of the $Fe_{70}Cu_{30}$ alloy (Fig. 5b), diffraction peaks related to the fcc Cu and the bcc Fe phase are observed after the first as well as after the second deformation step. The intensity of the Cu peaks increased somewhat after the second deformation step and the intensity of the Fe peaks is diminished at the same time. Furthermore, both sets of peaks show a broadening after the second deformation step. The Cu peaks are also slightly shifted to lower diffraction angles after the second deformation step. Similar results are obtained in the $Fe_{50}Cu_{50}$ alloy (Fig. 5c). In turn, a two-phase structure consisting of fcc Cu and bcc Fe is obtained at both deformation steps. The intensity of the Fe peaks after the second deformation step is again reduced whereas the intensity of the Cu peak is slightly increased. Moreover, broadening of the peaks after the second deformation step is observed as well. The position of the Cu peaks after the second deformation step is shifted to lower diffraction angles.

Generally, the Cu peaks in the X-ray diffraction pattern of the $Fe_{70}Cu_{30}$, $Fe_{50}Cu_{50}$ and $Fe_{15}Cu_{85}$ samples after the second deformation step are all shifted to lower diffraction angles. In the case of the $Fe_{85}Cu_{15}$ sample, the Fe peaks are shifted to lower diffraction angles. A two-phase structure is maintained in the $Fe_{70}Cu_{30}$ and $Fe_{50}Cu_{50}$ sample even after both processing steps are conducted. Based on the results

from the X-ray diffraction experiments it might be assumed that for Cu contents >30 wt.%, Cu supersaturated solid solutions are formed even if a complete single-phase structure is not obtained. For Fe contents >85%, Fe supersaturated solid solutions are achieved. A quantitative phase analysis was not done as the strongest composite peaks form close to the high-intensity peaks of Fe and Cu. These peaks are quite broadened and additionally there is still a $K_{\alpha 2}$ component in the incoming radiation causing considerable overlap. For the present case the disappearance of the peaks of the initial phases are good indicators of the creation and loss of the solid solution.

Atom probe analysis on the $Fe_{50}Cu_{50}$ sample was conducted to evaluate the possible formation of supersaturated solid solutions in the two-phase structures and to map the distribution of Fe and Cu atoms in a volume of $65 \times 66 \times 285$ nm^3 (Fig. 6a). Cu atoms are displayed in green and Fe atoms in blue, respectively. The Cu as well as the Fe concentration profile across a smaller analyzed volume is shown in Fig. 6b. Grain sizes of both phases around 10 nm can be estimated from this plot. The Cu as well as the Fe concentration profile exhibits gradients which might indicate Fe–Cu interdiffusion. The Cu concentration in the Fe phase is up to ~25 at.% and the Fe concentration in the Cu phase is up to ~20 at.%. Under equilibrium conditions, the mutual solubility of Fe and Cu is normally less than 0.1 at.% at room temperature. Therefore, these data confirm that the formation of Fe supersaturated solid solutions as well as Cu supersaturated solid solutions is simultaneously possible in the two-phase

structure. In contrast, no complete single-phase supersaturated solutions were obtained in Ref. [16], although it was shown that Fe clusters with a nanometer size are dissolved in Cu during HPT.

3.2. Thermal stability

In the following section, the thermal stability of the single-phase supersaturated solid solutions of the $Fe_{85}Cu_{15}$ and $Fe_{15}Cu_{85}$ samples are investigated. The samples are annealed at three different annealing temperatures for 1 h in air. To monitor a possible thermal decomposition process, the samples are investigated by X-ray diffraction after each annealing step. Furthermore, DSC measurements are conducted to determine the temperature of the decomposition process. Fig. 7 shows the X-ray diffraction patterns of the $Fe_{85}Cu_{15}$ and $Fe_{15}Cu_{85}$ alloys after annealing for 1 h at 290 °C, 440 °C and 620 °C and after the second deformation step without an annealing treatment as a reference (indicated as RT in the plot). After annealing for 1 h at 290 °C, the diffraction pattern of the $Fe_{15}Cu_{85}$ alloy sample consists of just Cu peaks. Not even an indication of peaks belonging to the bcc Fe phase is visible, showing that it is still fully resolved in Cu. Moreover, the width of the Cu peaks decreases, which might be due to thermal relaxation of the structure. With annealing at 440 °C, the bcc Fe phase peaks appear, which is a clear sign of the decomposition of the initial single fcc $Fe_{15}Cu_{85}$ phase into an fcc Cu and bcc Fe phase. After annealing at 620 °C, the X-ray diffraction pattern does not change very much. Fcc Cu as well as
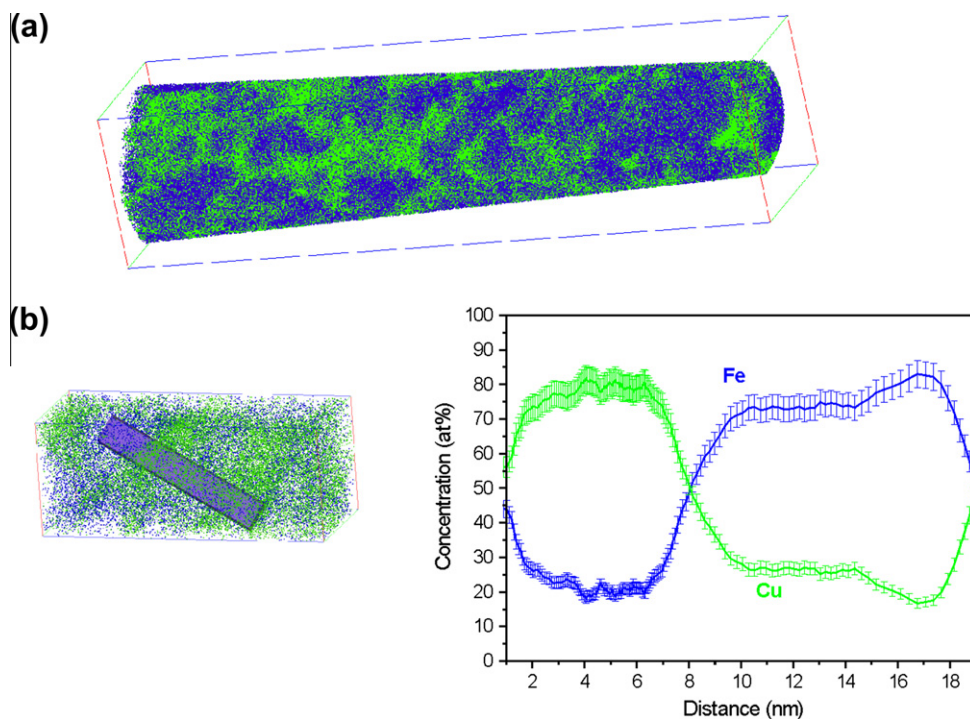

Fig. 6. Atom probe data of the $Fe_{50}Cu_{50}$ alloy after both deformation steps: (a) three-dimensional reconstructed volume ($65 \times 66 \times 285$ nm^3) where Cu atoms are displayed in green and Fe atoms in blue, respectively. (b) Cu concentration profile (green) and Fe concentration profile (blue) across the Cu/Fe interfaces. (For interpretation of the references to colour in this figure legend, the reader is referred to the web version of this article.)
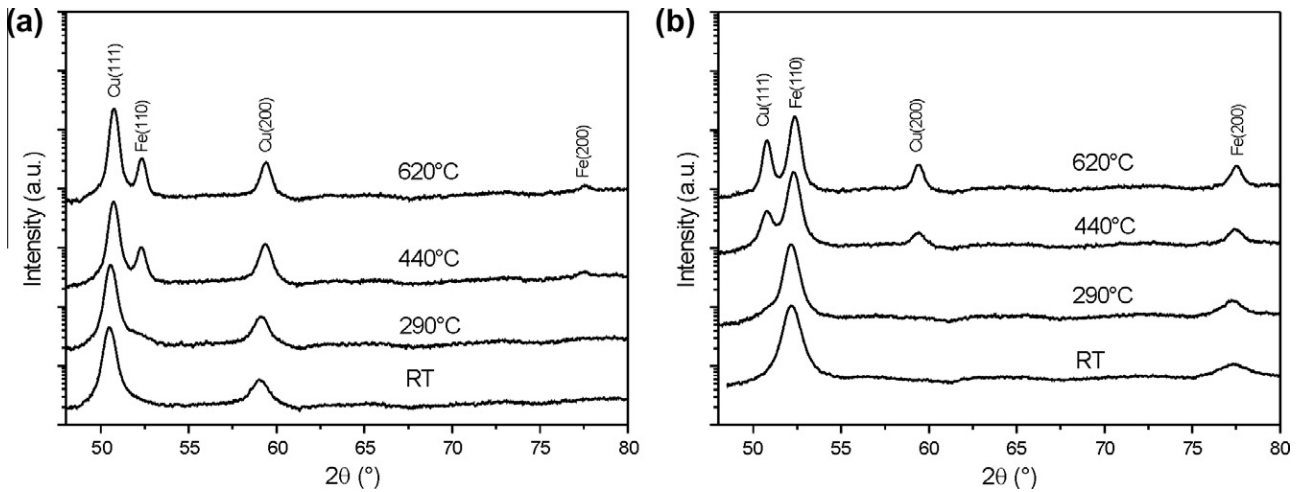
Fig. 7. X-ray diffraction patterns of the $Fe_{15}Cu_{85}$ alloy (a) and the $Fe_{85}Cu_{15}$ alloy (b) sample recorded in the as-deformed condition (both deformation steps) and after annealing for 1 h at 290 °C, 420 °C and 620 °C.

bcc Fe peaks are now visible, indicating that decomposition into a two-phase structure has occurred at annealing temperatures higher than 440 °C. With increasing annealing temperature, the Cu peaks are continuously shifted to higher diffraction angles, which are a further indication for the decomposition of the structure. The single-phase supersaturated solid solution is remained in the $Fe_{85}Cu_{15}$ alloy sample until annealing temperatures below 440 °C. After annealing at 440 °C for 1 h, Cu peaks appear in the X-ray diffraction pattern. Therefore, decomposition of the initial single bcc $Fe_{85}Cu_{15}$ phase into fcc Cu and bcc

Fe occurs. At an annealing temperature of 620 °C, bcc Fe and fcc Cu peaks are visible. Moreover, the slight shift of the Fe peaks to lower diffraction angles is reversed with increasing annealing temperature, which is again a further indication for the decomposition of the single-phase structure. Small thermal relaxation of the structure might also occur in this alloy at low annealing temperatures.

As an example, the microstructural evolution of the $Fe_{15}Cu_{85}$ sample with increasing annealing temperature is shown in Fig. 8. Compared to the as-deformed condition, no significant difference is visible between the microstruc-

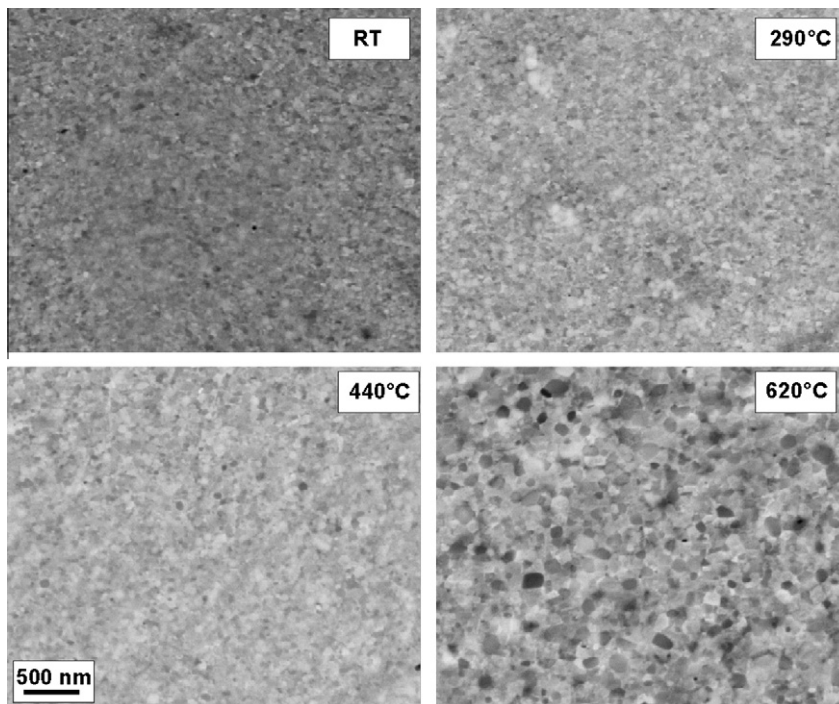Fig. 8. SEM micrographs (backscattered electron mode) showing the microstructure of the $Fe_{15}Cu_{85}$ alloy in the initial condition (RT) and after annealing for 1 h at 290 °C, 420 °C and 620 °C recorded at a radius of 3 mm in the tangential direction.

tures in the sample annealed at 290 °C and 440 °C. From the micrographs, no distinction between Fe and Cu grains can be made although a two-phase structure has already formed at 440 °C as confirmed by X-ray diffraction. At annealing temperatures of 620 °C, grain growth has occurred and grains with a size above 100 nm are visible. The microstructural evolution of the $Fe_{85}Cu_{15}$ sample is similar. Until annealing at the highest annealing temperature, no difference between the as-deformed and annealed microstructures is visible. No change in the grain size is observed after annealing for 1 h at 290 °C and 440 °C and from the micrographs it is not possible to distinguish between Fe and Cu grains. Only at the highest annealing temperature does marginal grain growth occur as well.

In Fig. 9, the microhardness as a function of annealing temperature of the $Fe_{85}Cu_{15}$ and $Fe_{15}Cu_{85}$ samples is plotted. In the $Fe_{85}Cu_{15}$ sample, the hardness increases with increasing annealing temperatures in the beginning. The hardness of the as-deformed sample is 639 HV whereas the hardness after annealing at 290 °C and 440 °C is 642 and 675 HV, respectively. At the highest annealing temperature, the hardness decreases and has a somewhat lower value compared to the as-deformed condition (576 HV). First of all there is a slight increase in the hardness in the $Fe_{15}Cu_{85}$ sample during annealing. The hardness of the as-deformed sample is 327 HV and the hardness after annealing at 290 °C is 330 HV. At 440 °C a higher hardness value of 337 HV compared to the initial condition is measured but at the highest annealing temperature the hardness decreases to 277 HV. In both samples, the measured hardness values are higher compared to the as-deformed condition if decomposition of the supersaturated solid solution has occurred. At the highest annealing temperature, the hardness of both samples decreased, which is due to the occurrence of marginal grain growth during the annealing treatment, as shown for example for the annealed $Fe_{15}Cu_{85}$ sample in Fig. 9.
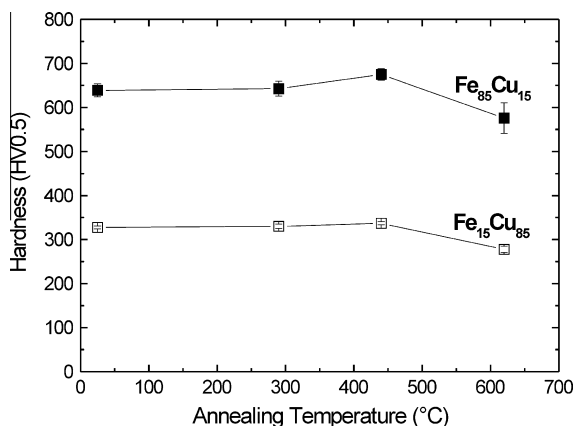

Fig. 9. Microhardness of the $Fe_{15}Cu_{85}$ alloy and the $Fe_{85}Cu_{15}$ alloy sample after annealing for 1 h at 290 °C, 420 °C and 620 °C. Mean values of 16 indents starting from a radius of 2 mm to the outer edge of the sample are reported.

DSC of the $Fe_{15}Cu_{85}$ sample shows a broad exothermic signal extending from 302 °C to 585 °C during heating from room temperature to higher temperatures. Integration of the area under the DSC curve yields a total stored energy of 43.9 J g^{-1} with a peak temperature of 434 °C. Such an exothermic event might be attributed to the transition from the metastable supersaturated phases to the stable two-phase structure, which fits well with the results obtained from the X-ray diffraction experiments. It indicates that the phase separation process is completed when reaching a temperature above 585 °C. In the case of the $Fe_{85}Cu_{15}$ sample, a smaller exothermic peak extending from 300 °C to 483 °C is observed, with a total stored energy of 13.1 J g^{-1} and a peak temperature of 385 °C. This is again attributed to the decomposition of the supersaturated phase to the stable elemental Fe and Cu phases, which starts at approximately the same temperature and is completed at a somewhat lower temperature of 480 °C than in the $Fe_{15}Cu_{85}$ sample.

4. Discussion

From the experiments it is concluded that three composition regions can be distinguished in the as-deformed state after the two-step HPT process: a nanocrystalline fcc supersaturated Cu phase at high Cu contents, a mixture of nanocrystalline supersaturated fcc Cu and bcc Fe phase for medium Cu contents and a nanocrystalline supersaturated bcc Fe phase for low Cu contents. Therefore, the formation of supersaturated solid solutions over the whole composition range occurs as a result of HPT deformation. After the first processing step, however, a two-phase ultrafine-grained material is formed. Depending on composition, the grain size of Cu is between 200 nm and 300 nm, and around 300 nm and 400 nm for Fe. After the second processing step, a much smaller grain size is reached. The nanocrystalline grain size obtained in the composites is significantly smaller compared to pure Fe and Cu deformed by SPD [25,26].

4.1. Why is a two-step process necessary?

If continuous shearing of the individual Fe and Cu powder components in the composite during HPT deformation and volume conservation is assumed, their thickness decreases with increasing applied deformation. If d_0 denotes the initial particle size and γ is the applied shear strain, their thickness d_1 after HPT deformation can be estimated for larger γ to be

$$d_1 = d_0/\gamma. \tag{1}$$

If powders with a mean initial particle size d_0 of ~50 μm (like the Cu powders in this study) are deformed to a shear strain of $\gamma = 100$, their thickness or their size after the deformation is about 500 nm. This result fits very well to the observed microstructures in the deformed composite materials where a two-phase structured mate-

rial is clearly observed in all compositions (Fig. 2). In the individual components of the composite, an ultrafine-grained microstructure is formed. With monotonic shear deformation like in the HPT process and equal channel angular pressing, very high amounts of deformation are necessary to reach ~2 nm distance between two phases, which are reported to be a basic requirement in the case of Fe for alloying of Fe and Cu and to initiate the formation of supersaturated solid solutions in the Fe–Cu system [14]. Using Eq. (1) and assuming $d_0 = 50$ μm to obtain a 2 nm spacing would require a γ of 20000. This is in principle possible by HPT but it is extraordinarily time- and energy-consuming. The large necessary strain becomes evident if one considers a lamellar structure and applies a simple shear in the direction parallel to the aligned lamellae. Such a shear does not change the lamellar spacing.

On account of this and to further increase the effectiveness of the deformation process, a novel two-step HPT process was developed (Fig. 10a). After the shear deformation is applied in one direction, new samples are fabricated out of these already deformed samples, which are further deformed by HPT. Due to the cutting process, a rotation of the shearing direction by 90° is also introduced. The shear direction and lamellar alignment are now perpendicular to each other. The thickness d_2 of the lamella of the individual components after both HPT deformation steps can now assumed to be

$$d_2 = d_1/\gamma_2 = d_0/(\gamma_1 \cdot \gamma_2) \tag{2}$$

where γ_1 denotes the applied shear strain in the first deformation step and γ_2 is the applied shear strain in the second deformation step. If now a shear strain of $\gamma_1 = 100$ is applied in the first HPT deformation step and a shear strain of $\gamma_2 = 100$ is applied in the second HPT deformation step, the final thickness of the individual components should become 5 nm or lower.

As an example for the effectiveness of the two-step HPT process, the microhardness of the $Fe_{85}Cu_{15}$ alloy sample is plotted in Fig. 10b. After the first processing step, nearly constant hardness values were measured across the radii of the disk. The Cu and Fe phases have nearly reached their specific saturation microstructure in the whole sample. Only in the immediate vicinity of the center is the applied γ insufficient to reach the saturation. However, this part could not be localized by the hardness measurements. The spacing between the two phases in the whole sample is larger than the saturation grain size of the individual phases. Therefore, the hardness is nearly constant. After the second processing step, a continuous increase of the hardness with increasing radii (i.e. increasing strain) is again observed.

Due to the fast decrease of the lamella spacing of the Fe and Cu phases the size of the grains in Cu and Fe become restricted by the fast decreasing lamella spacing. As a consequence the hardness increases with increasing γ_2, i.e. increasing radius.

4.2. The formation of supersaturated solid solutions

From free energy curves calculated by the CALPHAD method [13], it was shown that for a Fe content of $x > 80$, the free energy of the bcc structure is smaller whereas at Fe contents of $x < 40$, the fcc structure is more stable. In between, the difference of the free energy between both structures is small and the formation of both phases is favorable. This theoretical result fits quite well with our obtained structures in the FeCu system.

Different mechanisms were proposed in recent years of how the formation of a solid solution in immiscible systems with a positive heat of mixing can be explained during SPD. An explanation was given by Veltl et al. [27]: the driving force to form solid solutions comes from the energy stored in the grain boundaries in which a considerable amount of enthalpy can be stored in nanocrystalline metals. Jiang et al. [13], however, showed that the maximum increase in grain boundary enthalpy is not sufficiently high as compared to the free energy of mixing to explain the formation of solid solutions in the Fe–Cu system. Another explanation is a diffusion driven process. Raabe et al. [28], however, suggested that such a process can be excluded due to the lack of thermodynamic forces. The high number of introduced defects during SPD, like the high dislocation density, is proposed as another mechanism for the solid solution formation, which can be summarized as defect-enhanced diffusion processes [29–31]. The formation of a high number of non-equilibrium vacancies during SPD has been reported by a lot of researchers. Sauvage et al. [16] reported a very high vacancy production rate of 10^{-5} s^{-1} during HPT, which would increase the diffusion coefficient and furthermore enable the mechanical alloying of Fe and Cu. Nevertheless, the strain energy induced by mechanical deformation alone is not sufficient, as calculated in Ref. [10]. The defect-enhanced diffusion processes are proposed to be possible in Ref. [28], but the net flux depends on different defect densities and mobilities in the different phases.

Yavari et al. [14,32,33] proposed a different explanation for the occurrence of the formation of fcc solid solution in the Fe and Cu system. The free energy curve of a Fe component can be raised by the interfacial energy term [14]:

$$\Delta G_{int} = 3\gamma_{FeCu}V_m/r \tag{3}$$

where V_m is the molar volume and r is the radius of the particle. γ_{FeCu} is the interfacial energy between Fe–Cu interfaces. Therefore, if small Fe particles are formed the free energy curve of Fe is raised to higher values. This is accompanied with a change of the comment tangent with the free energy curve of the Cu phase to higher Fe contents and therefore to an enhancement of supersaturation. If elemental fragments with small tip radii below 2 nm are formed, capillary pressure forces the atoms which are on the tip of the fragments to dissolve. This process continues as long as such small fragments are continuously created. In mechanical alloying, the grain size of initial pure Cu fcc
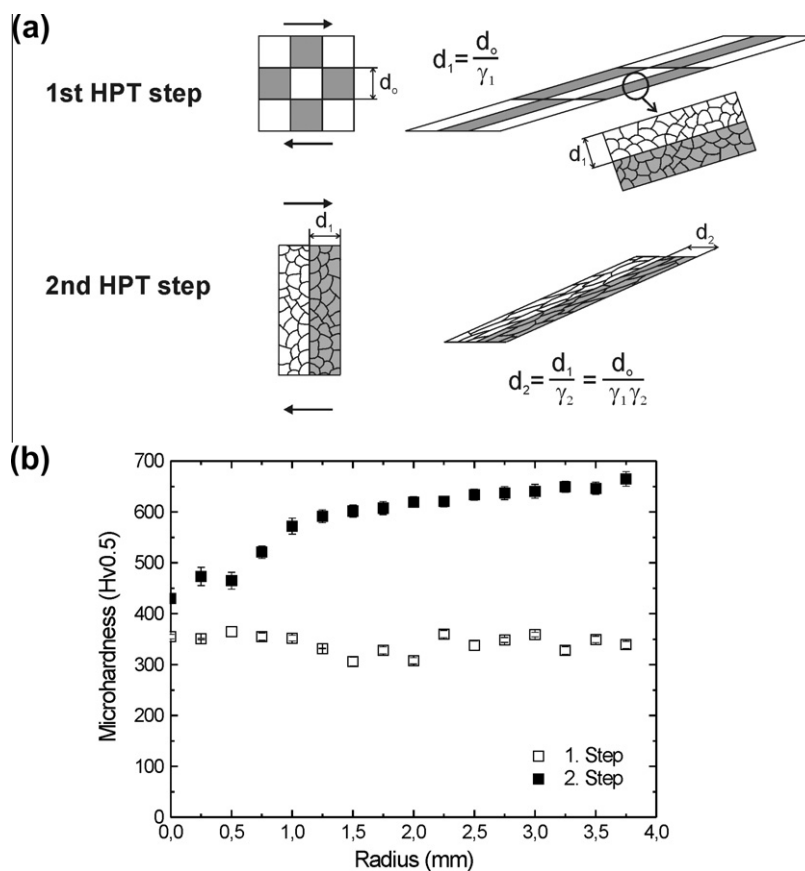
Fig. 10. (a) Schematic sketch showing the continuous shearing of the different components of the composite in the first and second deformation step. Between the different deformation steps, a rotation of the sample of 90° is included. (b) Microhardness of the $Fe_{85}Cu_{15}$ alloy sample after the first and second processing steps. Indents are made across the radii of the sample with a distance of 0.25 mm between the indents.

phase is reduced in the beginning to a value of about 20 nm and remains constant at higher milling times. The same happens with the initial pure Fe bcc phase which gets refined until a grain size of 10 nm before it disappears. Even if the overall grain size of the solid solution phase is ~10 nm, it might be possible that small fragments below 2 nm are formed again and again if the deformation continues. From the calculated energy stored in the Fe/Cu interface for an elemental size of 1 nm, formation of fcc solid solutions is energetically possible. The same processes might occur during HPT deformation. Sauvage et al. [16] showed that Fe clusters with a nanometer size are dissolved during HPT. The smaller the size of the Fe clusters, the higher the amount of dissolved Fe in Cu. Nonetheless, complete single-phase supersaturated solutions were not obtained in this work. The second processing step offers a new possibility to quickly obtain grain size regions where the formation of complete supersaturated solid solutions in the FeCu system are feasible.

Therefore, the enthalpy contribution of the Fe–Cu interfaces can act as a driving force for the solid solution formation, at least for fcc solid solutions [14,32,33]. It might be also an explanation for the bcc solid solution formation during SPD. Additional enthalpy which comes from the SPD is not included in this calculation. Therefore, the enthalpy contribution from the interface, together with a contribution from the deformation, might be large enough to overcome the positive heat of mixing of this alloy in the bcc region.

Another explanation is given in Ref. [28]: dislocation shear driven alloying is proposed to explain the mechanically induced mixing in normally immiscible systems. This process includes a dislocation-assisted carrier mechanism with multislip shear transfer on more than one slip system across heterophase interfaces. This mechanism is also known as dislocation shuffle mechanism [34].

4.3. The hardness evolution after annealing

Decomposition occurs during annealing above temperatures of 300 °C, which leads to the formation of a nanocrystalline FeCu composite material with an enhanced hardness and an extraordinary thermal stability. Even at high annealing temperatures, the nanocrystalline structure of the composite is retained and hardness values remain nearly constant. After decomposition, separated fcc and bcc phases exist in the composite. Due to this structural configuration, where grains of the one phase may be isolated from the other phase grain growth through boundary migration is reduced [35]. Another reason for the observed

high thermal stability may be impurities which are introduced in the latter bulk compacts from the as-received powders or from contamination during processing. Such impurities would furthermore retard grain boundary movement. However, due to the relative large initial powder size the content of impurities should be relatively small.

In general, the hardness of the FeCu composites in the as-deformed state increases with increasing Fe content after both processing steps. With a simple rule of mixture,

$$H_{\text{composite}} = H_{\text{Cu}} * F_{\text{Cu}} + H_{\text{Fe}} * F_{\text{Fe}} \qquad (4)$$

the upper bound of the hardness of the composite ($H_{\text{composite}}$) materials can also be calculated. For H_{Cu} and H_{Fe}, which denote the hardness of pure Cu and Fe with a similar grain size (∼15 nm), values of 153 and 693 HV are used [36,37]. F_{Cu} and F_{Fe} is the fraction of Cu and Fe in the composite. The predicted hardness values of the composites calculated with this rule of mixture are lower compared to the experimental ones in the case of the $Fe_{85}Cu_{15}$ and $Fe_{15}Cu_{85}$ samples. Therefore, solid solution hardening seems to take place although it is only reported to occur for Cu(Fe) alloys [38]. The experimental hardness of the $Fe_{50}Cu_{50}$ fits well to estimated ones but the experimental hardness of the $Fe_{70}Cu_{30}$ sample is too low. After decomposition of the single-phase FeCu composite structure ($Fe_{85}Cu_{15}$ and $Fe_{15}Cu_{85}$) and before grain growth during annealing sets in, an enhanced hardness compared to the as-deformed material is observed. The same behavior is observed in supersaturated CuCr composites [18]. In this case, solid solution softening in the as-deformed state was given as an explanation for the enhanced hardness in the annealed state. In our case, no solid solution softening occurred in the as-deformed samples. One explanation for the enhanced hardness after annealing in our study might be the additional strengthening from the interphase boundaries between the dissimilar bcc and fcc phases, as shown in Ref. [39], which are formed right after decomposition. Nevertheless, further investigations regarding the hardness phenomena have to be conducted to explain the details of the observed phenomena in future.

5. Conclusion

Bulk nanostructured FeCu alloys are prepared by a two-step HPT deformation process. In all alloys fcc and bcc solid solutions which are far from equilibrium are formed with this new two-step SPD technique similar to ball milling. After the first processing step, an ultrafine-grained two-phase composite material is formed. After the second deformation step, nanostructured supersaturated solid solutions were achieved. It was shown that mechanical intermixing of Fe and Cu is possible with SPD. The decomposition of the supersaturated solid solutions upon annealing is used to produce in situ two-phase nanocrystalline homogeneous FeCu composites. The FeCu composites after annealing show an enhanced hardness as well as a high thermal stability.

The advantages of the newly developed process are an uncomplicated control of the composition of the alloy, the possible combination of arbitrary material combinations, the easy production process and a high-quality final product which is already in bulk form.

References

[1] Di Maggio R, Ischia G, Rossi F, Molinari A, Bortolotti M. J Mater Sci 2007;42:9284.
[2] Kakisawa H. Mater Sci Eng A 2003;340:175.
[3] Ma E. Prog Mater Sci 2005;50:413.
[4] Johnson WL. Prog Mater Sci 1986;30:81.
[5] Koch CC. In: Cahn RW, Haasen P, Kramer EJ, editors. Materials science and technology. Weinheim: VCH; 1991.
[6] Oehring MY, Klassen T, Bormann R. Phys Status Solidi 1992;131:671.
[7] Eckert J, Holzer JC, Krill CE, Johnson WL. J Appl Phys 1993;73:2794.
[8] Fultz B, Ahn CC, Spooner S, Hong LB, Eckert J, Johnson WL. Metall Mater Trans A 1996;27:2934.
[9] Uenishi K, Kobayashi KF, Nasu S, Hatano H, Ishihara KN, Shingu PH. Z Metall 1992;83:132.
[10] Ma E, Atzmon MJ, Pinkerton FE. Appl Phys 1993;74:955.
[11] Jiang JZ, Gonser U, Gente C, Bormann R. Appl Phys Lett 1993;63:2768.
[12] Huang JY, Yu YD, Wu YK, Ye HQ, Dong ZF. J Mater Res 1996;11:2717.
[13] Jiang JZ, Gente C, Bormann R. Mater Sci Eng A 1998;242:268.
[14] Yavari AR, Desre PJ, Benameur T. Phys Rev Lett 1992;68:2235.
[15] Quelennec X, Menand A, Le Breton JM, Pippan R, Sauvage X. Philos Mag 2010;90:1179.
[16] Sauvage X, Wetscher F, Pareige P. Acta Mater 2005;53:2127.
[17] Valiev RZ, Islamgaliev RK, Alexandrov IV. Prog Mater Sci 2000;45:103.
[18] Sauvage X, Jessner P, Vurpillot F, Pippan R. Scripta Mater 2008;58:1125.
[19] Gorria P, Martínez-Blanco D, Blanco JA, Pérez MJ, Hernando A, Barquín LF, et al. Phys Rev B 2005;72:014401.
[20] Gorria P, Martínez-Blanco D, Iglesias R, Palacios SL, Pérez MJ, Blanco JA, et al. J Magn Magn Mater 2005;300:229.
[21] Gorria P, Martínez-Blanco D, Blanco JA, Pérez MJ, González MA, Campo J. Physica B 2006;384:336.
[22] Hohenwarter A, Bachmaier A, Gludovatz B, Scheriau S, Pippan R. Int J Mater Res 2009;100:1653.
[23] Pippan R, Wetscher F, Hafok M, Vorhauer A, Sabirov I. Adv Eng Mater 2006;8:1046.
[24] Pippan R, Scheriau S, Taylor A, Hafok M, Hohenwarter A, Bachmaier A. Annu Rev Mater Res 2010;40:319.
[25] Park K-T, Shin DH. Mater Sci Eng A 2002;334:79.
[26] Islamgaliev RK, Buchgraber W, Kolobov YR, Amirkhanov NM, Sergueeva AV, Ivanov KV, et al. Mater Sci Eng A 2001;319–321:872.
[27] Veltl G, Scholz B, Kunze HD. Mater Sci Eng A 1991;134:1410.
[28] Raabe D, Choi PP, Li YJ, Kostka A, Sauvage X, Lecoturier F, et al. MRS Bull 2010;35:982.
[29] Mazzone G, Antisari MV. Phys Rev B 1996;54:441.
[30] Mazzone G, Montone A, Vittori Antisari M, Angiolini M. Mater Sci Forum 1997;235:175.

[31] Angiolini M, Cardellini F, Krasnowski M, Mazzone G, Montone A, VittoriAntisari M. Microsc Microcanal 1995;6:601.

[32] Yavari AR. Mater Trans 1995;36:228.

[33] Yavari AR. Mater Sci Eng A 1994;179–180:20.

[34] Raabe D, Ohsaki S, Hono K. Acta Mater 2009;57:5254.

[35] Schaffer G. Scripta Metall Mater 1992;27:1.

[36] Nieman GW, Weertman JR, Siegel RW. J Mater Res 1991;6:1012.

[37] Jang JSC, Koch CC. Scripta Metall Mater 1990;24:1599.

[38] Shen TD, Koch CC. Acta Mater 1996;44:753.

[39] He L, Ma E. Nanostruct Mater 1996;7:327.